



2-D WFS Approach Through Field Transformation-Application to Performance Prediction in Standard Antenna Simulators

Manouan Aka Constant Niamien

► To cite this version:

Manouan Aka Constant Niamien. 2-D WFS Approach Through Field Transformation-Application to Performance Prediction in Standard Antenna Simulators. IEEE Open Journal of Antennas and Propagation, 2021, 2, pp.1120-1131. 10.1109/OJAP.2021.3127315 . hal-03541372

HAL Id: hal-03541372

<https://normandie-univ.hal.science/hal-03541372>

Submitted on 4 Jun 2024

HAL is a multi-disciplinary open access archive for the deposit and dissemination of scientific research documents, whether they are published or not. The documents may come from teaching and research institutions in France or abroad, or from public or private research centers.

L'archive ouverte pluridisciplinaire **HAL**, est destinée au dépôt et à la diffusion de documents scientifiques de niveau recherche, publiés ou non, émanant des établissements d'enseignement et de recherche français ou étrangers, des laboratoires publics ou privés.



Distributed under a Creative Commons Attribution 4.0 International License

2-D WFS Approach Through Field Transformation—Application to Performance Prediction in Standard Antenna Simulators

CONSTANT M. A. NIAMIEN¹ (Member, IEEE)

Research Institute of Embedded Electronic Systems, Normandie Université, UNIROUEN, ESIGEEC, IRSEEM, 76000 Rouen, France

CORRESPONDING AUTHOR: C. M. A. NIAMIEN (e-mail: constant.niamien@esigelec.fr)

This work is carried out as part of project SURFAS, an Interreg France (Channel) England cross-border cooperation project. The project is cofinanced by ERDF.

ABSTRACT This paper presents a 2-D wavefield synthesis approach directly implementable in standard antenna simulation software. The approach uses a field transformation matrix and two array sets to design vertically and horizontally polarized wavefields, implemented with thin electric dipoles for their simple geometry. The synthesized wavefields positively correlate with numerical methods (FIT, FEM) obtained from full-wave simulations over various array sets (size, number, polarization, frequency). Synthesizing 2-D isotropic wavefields in both polarizations under an error vector magnitude (EVM) equal to or smaller than -30 dB is demonstrated over the largest test zone radius of $\lambda/10$ with just three dipoles located at a minimum distance of 5λ far from the phase center. Application to a test antenna (folded dipole) anticipates the received power and MEG directly inside the antenna simulator in receiving mode. This valuable design option, not handled by most antenna simulators, helps optimize the antenna with the propagation medium characteristics during the design stage.

INDEX TERMS Antenna arrays, dipole antennas, electromagnetic propagation, wavefield synthesis.

I. INTRODUCTION

SYNTHESIZING a controlled electromagnetic environment is attractive for general antenna characterization. This often demands precise propagation medium characteristics set by the field amplitude and space-time distributions, power density, incidence angle, etc. In practice, one often encounters wavefield synthesis approaches through antenna pattern and gain measurement systems performed in standard anechoic chambers. A far-zone transmitting antenna illuminates a rotating antenna under test (AUT) with an incident plane wave [1, pp. 1024–1033]. This setup creates a limited number of incidences at the AUT's level, typically only one, for an ideal Dirac-directive transmitting antenna. Instead, a reverberation chamber can provide multiple incidences to form a three-dimensional (3-D) statistically isotropic wavefield [2], not purely isotropic in space. Over-the-Air (OTA) approaches as the multi-probe anechoic chamber (MPAC) methods can create multi-incident plane waves over a 2-D test zone based on a set of uniformly distributed transmitting antennas arranged

in the azimuthal plane [3]–[7]. These approaches offer advanced testing capabilities as the channel throughput and model at the expense of increased complexity and cost due to the number of parameters and devices to set up. Overall, practical wavefield synthesis approaches can provide a 2-D or 3-D test zone under multiple incidences but are complex to set up, cumbersome, and not affordable.

Theoretical OTA approaches offer another option to synthesize a 2-D test zone as the works in [6]–[7], considering a 3-D set of several transmitting antennas (more than 29) distributed over one hemisphere according to Lebedev and Tchebyshev grids. These approaches show an attractive isotropic field accuracy. Still, they remain complex and challenging to validate experimentally or numerically using standard electromagnetic (EM) simulation software due to the number of antennas used over a 3-D spatial arrangement.

This paper presents a 2-D wavefield synthesis approach directly implementable in standard antenna simulation software. The approach uses a field transformation matrix to turn the radiation of several transmitting antennas into receiving

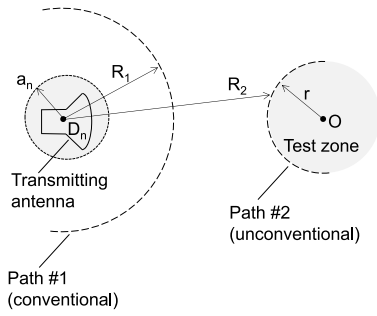


FIGURE 1. Overview of the problem formulation.

mode. Thin electric dipoles are used for their simple geometry to design the wavefields with horizontal and vertical polarizations. The theoretical results are validated numerically with full-wave simulations over various array sets (size, number, polarization, frequency). The optimum parameters that synthesize the largest 2-D isotropic test zone are derived and applied to a practical antenna case (AUT) within a standard antenna simulator. The benefits of this application are twofold:

- i) The wavefield synthesis array and the AUT are integrated into the full-wave simulator to include all propagation and interaction phenomena, leading to more realistic and rigorous results.
- ii) The received power is accurately anticipated even under multiple incidences.

This performance prediction, not handled by most antenna simulators, is demonstrated to the author's best knowledge for the first time. This option is essential for optimizing the general antenna at the design stage while including the propagation medium characteristics.

This paper is organized as follows. Section II formulates the problem of the field transformation and details the proposed approach. Section III implements the approach with thin electric dipoles, while Section IV validates it numerically with full-wave simulations for various array sets (size, number, polarization, frequency). Section V discusses and derives the optimum parameters providing the largest isotropic test zone. Finally, Section VI applies the synthesized isotropic wavefield to a test antenna (folded dipole) for performance prediction in the context of ambient RF energy harvesting.

II. FORMULATION

A. OVERVIEW OF THE PROBLEM

Let us consider an arbitrary transmitting antenna located at point D_n and surrounded by the smallest virtual sphere of radius a_n , as depicted in Fig. 1. The objective is to formulate this antenna's radiation over a limited space region, designated as the test zone, bounded by path #2. This problem may be analyzed from two viewpoints.

In the transmitting viewpoint, typically from the source at point D_n , the radiated wavefronts describe outgoing spherical waves (paths), concave and similar to path #1. Therefore,

the field over path #1 coincides with the far-field pattern of the transmitting antenna under $R_1 \geq 2(2a_n)^2/\lambda$, λ being the free-space wavelength. This pattern is well documented in the literature for several conventional antennas [1]. Since path #1 is concave while path #2 is convex, one will have to design a specific field transformation to get the far-field pattern over path #2. This is not necessarily straightforward due to an increased degree of freedom since radius R_2 varies over path #2. It is worth mentioning that invoking the reciprocity theorem will increase complexity by needing a second antenna (probe) to move on path #2 or using an array of probes on path #2, all directed toward point D_n [1, p. 148].

In the receiving viewpoint, typically at the receiver's location at point O, path #2 is seen concave with a fixed radius r . Thus, this configuration provides several advantages:

- i) A reduced degree of freedom in analyzing the field (on path #2) under a constant observation radius r .
- ii) Path #2 is similar to the spherical wavefronts that any test antenna located at point O would radiate. This simplifies the field components' analysis.
- iii) For the case of several distributed transmitting antennas, it is physically meaningful to analyze the total field from the focal point whether it exists (here, point O).

The above explanations justify adopting the receiving viewpoint, which designs the field over the test zone in the receiving coordinate system located at point O.

B. FIELD TRANSFORMATION APPROACH

Let us consider an array of N transmitting antennas located over a spherical surface and radiating broadside toward point O (focal point), which is also the phase center that may host a receiving antenna under test (AUT), as depicted in Fig. 2a. The n^{th} antenna element of this array is located at point D_n and arbitrarily oriented in space for the general formulation, as depicted in Fig. 2b.

Since most antennas radiate spherical waves with a negligible radial field component (assumed throughout the paper), the far-field pattern of the general antenna element can be written in the local spherical coordinate system ($D_n, \mathbf{e}_r, \mathbf{e}_\theta, \mathbf{e}_\phi$) as:

$$\mathbf{F}_n \approx F_{\theta_n}(\Omega_n)\mathbf{e}_{\theta_n} + F_{\phi_n}(\Omega_n)\mathbf{e}_{\phi_n} \quad (1)$$

where subscript n varies from 1 up to N , Ω_n is the solid angle at the observation point M seen in the local system with the spherical coordinates (r_n, θ_n, ϕ_n) , letter F represents both the electric (E) and magnetic (H) fields. Throughout this paper, boldface letters denote vectors.

Equation (1) formulates the radiation of the n^{th} antenna element seen locally, that is, within the transmitting spherical system ($D_n, \mathbf{e}_r, \mathbf{e}_\theta, \mathbf{e}_\phi$). The objective is to transform this pattern into the receiving spherical coordinate system (O, $\mathbf{e}_r, \mathbf{e}_\theta, \mathbf{e}_\phi$) taken as the reference one. This field transformation requires three key steps detailed in Fig. 3.

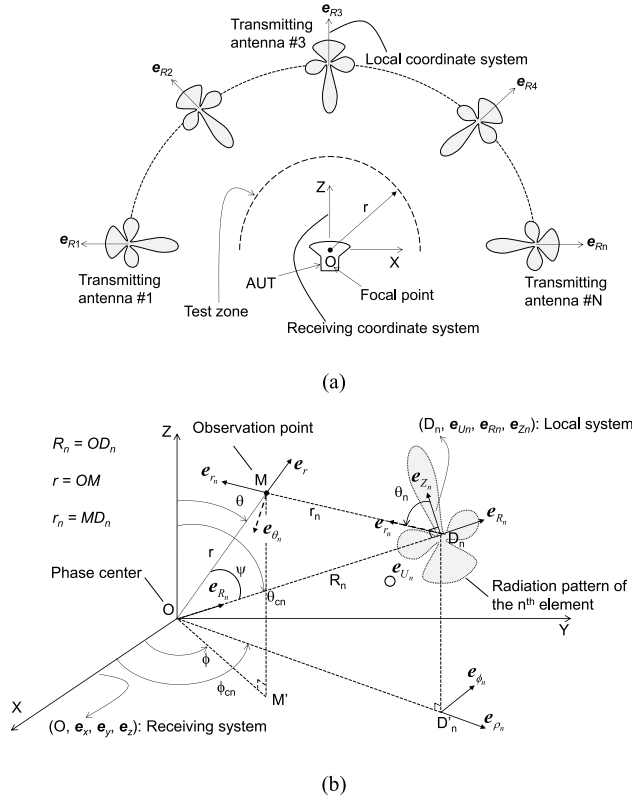


FIGURE 2. Test zone creation with (a) an array of N radiating elements, (b) case of a single radiating antenna within a general representation.

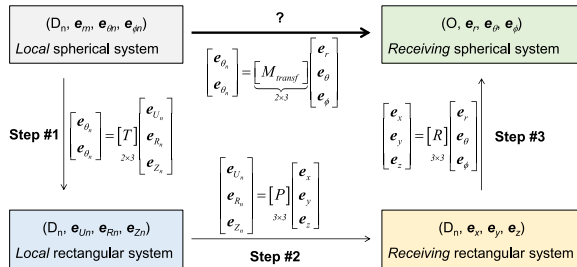


FIGURE 3. Mechanism of the field transformation approach.

1) STEP #1 (SPHERICAL-TO-RECTANGULAR LOCAL BASE TRANSFORMATION)

Let us consider the transmitting local rectangular coordinate system $(D_n, \mathbf{e}_{Un}, \mathbf{e}_{Rn}, \mathbf{e}_{Zn})$ referenced at point D_n . The unit vector \mathbf{e}_{Rn} is explicitly oriented in the radial direction (OD_n) to simplify the local system's spatial orientation.

The first step consists of expressing the spherical base $(\mathbf{e}_n, \mathbf{e}_n)$ into the rectangular one $(\mathbf{e}_{Un}, \mathbf{e}_{Rn}, \mathbf{e}_{Zn})$ locally using the following relationships based on Fig. 2b:

$$\mathbf{e}_{\theta n} = \cos \theta_n \mathbf{e}_{\rho n} - \sin \theta_n \mathbf{e}_{Zn} \quad (2a)$$

$$\mathbf{e}_{\phi n} = -\sin \phi_n \mathbf{e}_{Un} + \cos \phi_n \mathbf{e}_{Rn} \quad (2b)$$

where vectors $\mathbf{e}_{\rho n}$ and \mathbf{e}_{rn} are defined by:

$$\mathbf{e}_{\rho n} = \frac{\mathbf{e}_{rn} - \cos \theta_n \mathbf{e}_{Zn}}{\sin \theta_n} \quad (2c)$$

$$\mathbf{e}_{rn} = \frac{-R_n \mathbf{e}_{Rn} + r \mathbf{e}_r}{r_n} \quad (2d)$$

$$\mathbf{e}_r = \sin \theta \cos \phi \mathbf{e}_x + \sin \theta \sin \phi \mathbf{e}_y + \cos \theta \mathbf{e}_z \quad (2e)$$

Formatting (2a) – (2e) into a compact form leads to:

$$\begin{bmatrix} \mathbf{e}_{\theta n} \\ \mathbf{e}_{\phi n} \end{bmatrix} = \underbrace{\begin{bmatrix} 0 & -\frac{R_n}{r_n} \cot \theta_n & -(\sin \theta_n + \cot \theta_n \cos \theta_n) \\ -\sin \phi_n & \cos \phi_n & 0 \end{bmatrix}}_{[T_1]} \times \underbrace{\begin{bmatrix} \mathbf{e}_{Un} \\ \mathbf{e}_{Rn} \\ \mathbf{e}_{Zn} \end{bmatrix}}_{[T_0]} + \underbrace{\begin{bmatrix} \frac{r}{r_n} \cot \theta_n & 0 & 0 \\ 0 & 0 & 0 \end{bmatrix}}_{[T_0]} \begin{bmatrix} \mathbf{e}_r \\ \mathbf{e}_\theta \\ \mathbf{e}_\phi \end{bmatrix} \quad (3)$$

where $[T_1]$ and $[T_0]$ are 2×3 -scalar matrices, $R_n = OD_n$, $r = OM$, the spherical angles (θ_n, ϕ_n) are defined later on.

2) STEP #2 (RECTANGULAR-TO-RECTANGULAR BASE TRANSFORMATION)

The second step consists of expressing the transmitting rectangular base vectors $(\mathbf{e}_{Un}, \mathbf{e}_{Rn}, \mathbf{e}_{Zn})$ into the receiving ones $(\mathbf{e}_x, \mathbf{e}_y, \mathbf{e}_z)$ using the following relationships:

$$\mathbf{e}_{Rn} = \sin \theta_{cn} \cos \phi_{cn} \mathbf{e}_x + \sin \theta_{cn} \sin \phi_{cn} \mathbf{e}_y + \cos \theta_{cn} \mathbf{e}_z \quad (4a)$$

$$\mathbf{e}_{Zn} = \sin \theta_{en} \cos \phi_{en} \mathbf{e}_x + \sin \theta_{en} \sin \phi_{en} \mathbf{e}_y + \cos \theta_{en} \mathbf{e}_z \quad (4b)$$

$$\mathbf{e}_{Un} = \mathbf{e}_{Rn} \times \mathbf{e}_{Zn} \quad (4c)$$

where (θ_{cn}, ϕ_{cn}) and (θ_{en}, ϕ_{en}) denote the spherical angles attached to point D_n and unit vector \mathbf{e}_{Zn} , respectively, seen in the receiving system $(O, \mathbf{e}_x, \mathbf{e}_y, \mathbf{e}_z)$.

Formatting (4a) – (4c) into a matrix form leads to:

$$\begin{bmatrix} \mathbf{e}_{Un} \\ \mathbf{e}_{Rn} \\ \mathbf{e}_{Zn} \end{bmatrix} = \underbrace{\begin{bmatrix} |e_{Rny} \ e_{Rnz}| & -|e_{Rnx} \ e_{Rnz}| & |e_{Rnx} \ e_{Rny}| \\ |e_{Zny} \ e_{Znz}| & -|e_{Znx} \ e_{Znz}| & |e_{Znx} \ e_{Zny}| \\ e_{Rnx} & e_{Rny} & e_{Rnz} \\ e_{Znx} & e_{Zny} & e_{Znz} \end{bmatrix}}_{[P]} \times \begin{bmatrix} \mathbf{e}_x \\ \mathbf{e}_y \\ \mathbf{e}_z \end{bmatrix} \quad (5)$$

where $[P]$ is a 3×3 -matrix whose elements are the components of vectors \mathbf{e}_{Rn} and \mathbf{e}_{Zn} , obtained from (4a) – (4b), while symbol $||$ means taking the determinant.

3) STEP #3 (RECTANGULAR-TO-SPHERICAL BASE TRANSFORMATION)

The third step consists of expressing the rectangular base $(\mathbf{e}_x, \mathbf{e}_y, \mathbf{e}_z)$ into the spherical one $(\mathbf{e}_r, \mathbf{e}_\theta, \mathbf{e}_\phi)$ in the receiving system using a conventional matrix transformation:

$$\begin{bmatrix} \mathbf{e}_x \\ \mathbf{e}_y \\ \mathbf{e}_z \end{bmatrix} = \underbrace{\begin{bmatrix} \sin \theta \cos \phi & \cos \theta \cos \phi & -\sin \phi \\ \sin \theta \sin \phi & \cos \theta \sin \phi & \cos \phi \\ \cos \theta & -\sin \theta & 0 \end{bmatrix}}_{[R]} \begin{bmatrix} \mathbf{e}_r \\ \mathbf{e}_\theta \\ \mathbf{e}_\phi \end{bmatrix} \quad (6)$$

where $[R]$ is a 3×3 -matrix [1, p. 1084], and the spherical angles (θ, ϕ) are attached to the observation point M seen in the receiving system $(O, \mathbf{e}_x, \mathbf{e}_y, \mathbf{e}_z)$.

C. TOTAL FIELD VECTOR

The field vector \mathbf{F} at the observation point $M(r, \theta, \phi)$ seen in the receiving spherical system for the array of N transmitting antennas is written as the sum of each antenna's radiated field vector as:

$$\mathbf{F} = \sum_{n=1}^N \mathbf{F}_n = \sum_{n=1}^N \begin{bmatrix} F_{\theta n}(\Omega_n) \\ F_{\phi n}(\Omega_n) \end{bmatrix}^T \underbrace{\{[T_1][P][R] + [T_0]\}}_{[M_{\text{Transf}}]} \begin{bmatrix} \mathbf{e}_r \\ \mathbf{e}_\theta \\ \mathbf{e}_\phi \end{bmatrix} \quad (7)$$

where superscript T means transposition, $[M_{\text{Transf}}] = [T_1][P][R] + [T_0]$ is a 2x3-matrix transforming each antenna's pattern ($F_{\theta n}$, $F_{\phi n}$) from the transmitting to the receiving spherical bases.

Matrix $[T]$ reported in Fig. 3 is obtained as $[T] = [T_1] + [T_0][R]^{-1}[P]^{-1}$ since both $[R]$ and $[P]$ are non-singular, then invertible.

It is worth mentioning that (7) includes the coupling between the transmitting antennas as long as each antenna's radiation pattern ($F_{\theta n}$, $F_{\phi n}$) is taken in the lattice.

D. COMPUTATION

There are 11 unknowns in $[M_{\text{Transf}}]$, typically (r_n, θ_n, ϕ_n) , (r, θ, ϕ) , (θ_{cn}, ϕ_{cn}) , (θ_{en}, ϕ_{en}) , and R_n . These unknowns decrease to 8 by expressing (r_n, θ_n, ϕ_n) with (r, θ, ϕ) through the following relationships to compute in the receiving system ($O, \mathbf{e}_x, \mathbf{e}_y, \mathbf{e}_z$):

$$r_n = R_n \sqrt{1 + \frac{r^2}{R_n^2} - \frac{2r}{R_n} \cos \psi} \quad (8a)$$

$$\cos \psi = \mathbf{e}_{R_n} \cdot \mathbf{e}_r \quad (8b)$$

$$\sin \theta_n = |\mathbf{e}_{Z_n} \times \mathbf{e}_{r_n}| \quad (9a)$$

$$\cos \theta_n = \mathbf{e}_{Z_n} \cdot \mathbf{e}_{r_n} \quad (9b)$$

$$\sin \phi_n = |\mathbf{e}_{U_n} \times \mathbf{e}_{\rho_n}| \quad (10a)$$

$$\cos \phi_n = \mathbf{e}_{U_n} \cdot \mathbf{e}_{\rho_n} \quad (10b)$$

where symbol $||$ in (9a) and (10a) means taking the magnitude, while symbols “.” and “ \times ” represent the dot and cross products, respectively.

Computing (7) based on (8a) – (10b) requires knowing each transmitting antenna's position through point D_n ($R_n, \theta_{cn}, \phi_{cn}$), and vector \mathbf{e}_{Z_n} whose coordinates are (θ_{en}, ϕ_{en}) , all referenced in the receiving system ($O, \mathbf{e}_x, \mathbf{e}_y, \mathbf{e}_z$). The remaining unknowns (r, θ, ϕ) entirely determine the test zone's geometry through the observation point M . Fig. 4 summarizes the entire computation scheme starting with knowing each transmitting antenna's radiation pattern ($F_{\theta n}$, $F_{\phi n}$) in the local system ($D_n, \mathbf{e}_{rn}, \mathbf{e}_{\theta n}, \mathbf{e}_{\phi n}$).

The following section implements the approach with an array of electric dipoles.

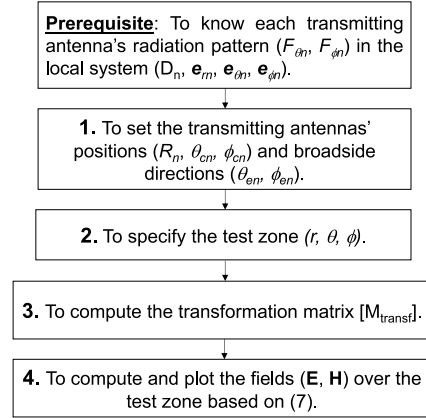


FIGURE 4. Computation scheme of the fields over the test zone.

III. IMPLEMENTATION WITH AN ARRAY OF DIPOLES

Let us implement the proposed approach with an array of N dipoles being the transmitting antennas. The motivations for using the dipole antenna include its simple geometry and well-known radiation characteristics. The former feature is essential to speed up full-wave implementations even though other antenna kinds may be successful.

A. THEORETICAL RADIATION OF A FINITE-LENGTH THIN DIPOLE

According to [1, p. 172], the electric and magnetic far-fields radiated by a finite-length thin dipole within the local spherical system ($D_n, \mathbf{e}_{rn}, \mathbf{e}_{\theta n}, \mathbf{e}_{\phi n}$) is written as:

$$\mathbf{E}_n \approx E_{\theta n} \mathbf{e}_{\theta n} = C_E \frac{I_n \cos\left(\frac{kL}{2} \cos \theta_n\right) - \cos\left(\frac{kL}{2}\right)}{r_n \sin \theta_n} e^{-jkr_n} \mathbf{e}_{\theta n} \quad (11a)$$

$$\mathbf{H}_n \approx H_{\phi n} \mathbf{e}_{\phi n} = \frac{E_{\theta n}}{\eta} \mathbf{e}_{\phi n} \quad (11b)$$

where L is the dipole's length, $\eta = 120\pi$, I_n is the current's maximum, $k = 2\pi/\lambda$ is the free-space propagation constant, λ is the free-space wavelength, $C_E = j\eta/2\pi = 60j$ is a complex coefficient (parameter j being the conventional complex number).

In (11a) and (11b), the dipole's center and axis coincide with point D_n and vector \mathbf{e}_{Z_n} , respectively.

B. SIMULATION-BASED RADIATION OF AN ARBITRARY DIPOLE

One may consider the radiation pattern of an arbitrary dipole antenna to synthesize the wavefield. In this case, the designer needs to simulate the dipole in transmitting mode, solely if the mutual coupling is negligible or in the lattice, if not, to get its radiation pattern $|F_{sn}(\Omega_n)|$ over the desired space region (Ω_n), s denoting r, θ , and ϕ . Thus, the dipole's complex radiated field is written under a spherical wave-mode assumption, as:

$$F_{sn}(\Omega_n) = |F_{sn}(\Omega_n)| e^{-jkr_n}. \quad (12)$$

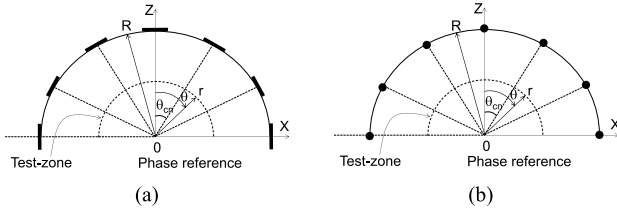


FIGURE 5. Wavefield synthesis sets with an array of dipoles, (a): vertical polarization (θ), and (b): horizontal polarization (ϕ).

TABLE 1. Coordinates of the dipoles' center positions.

$\theta_{cn} = -\frac{\pi}{2} + \frac{n-1}{N-1}\pi$	$\theta_{cn} < 0$	$\theta_{cn} \geq 0$
$\phi_{cn} = \pi$	π	0

Angle θ_{cn} ranges for $1 \leq n \leq N$. Arbitrarily, the first antenna ($n = 1$) is set on the negative x -axis ($x < 0$) with $\theta_{c1} = -\pi/2$.

It is worth mentioning that this procedure applies to any antenna type knowing its orientation in the local coordinate system. However, implementing (12) may require extensive computing resources (memory, speed) in practice to accelerate the computation (Fig. 4) for a conveniently discretized space region. For this reason, the theoretical formulas in (11) will be preferred over (12) to speed up the calculation since both data lead to the same results.

C. WAVEFIELD SETS

Let us consider several electrically identical dipoles to synthesize the wavefield over the test zone under the following considerations:

- The dipoles are fed in-phase with equal amplitude, consistent with a constant current in (11a).
- The dipoles are located on a circular path of radius R belonging to the upper hemisphere $z \geq 0$, hence $R_n = R$.
- The inter-element spacing between the dipoles is constant. Consideration of both a reasonable number of dipoles (N) and infinitesimal ($L \leq \lambda/50$) or short ($\lambda/50 < L \leq \lambda/10$) dipoles helps maintain a negligible coupling between the dipoles. On this basis, (11a) – (11b) still stands for the dipole taken in the lattice.
- The dipoles are oriented in space such that their broad-side patterns are directed toward the phase center, point O . Two sets are considered, as seen in Fig. 5.

In the first set, as seen in Fig. 5a, the dipoles are tangential to the circular line source and lie in the zx -plane. This set intends to synthesize a vertically polarized wavefield, also denoted as θ -polarization throughout the paper.

In the second set depicted in Fig. 5b, the dipoles are 90° -rotated along their radial axes (OD_n) to synthesize a horizontally polarized wavefield, denoted as ϕ -polarization throughout the paper. In this set, the dipoles are all directed along the y -axis. These two array sets specify the values of angles (θ_{cn} , ϕ_{cn}) and (θ_{en} , ϕ_{en}) for both polarizations, as seen in Tables 1 and 2.

TABLE 2. Coordinates of vector e_{zn} in the receiving rectangular system.

Wavefield	θ -polarized	ϕ -polarized
θ_{en}	$\theta_{cn} - \pi/2$	$\pi/2$
ϕ_{en}	0	$\pi/2$

TABLE 3. Electrical sizes of the source and test zone radii.

Frequency (GHz)	0.4	0.8	1.2
Dipole length (L)	$\lambda/250$	$\lambda/125$	$3\lambda/250$
Source radius (R)	λ	2λ	3λ
Test zone radius ($r = 0.1R$)	$\lambda/10$	$\lambda/5$	$3\lambda/10$
$k R - r $	$9\pi/5$	$18\pi/5$	$27\pi/5$

$k = 2\pi/\lambda$ is the free space propagation constant, λ being the free space wavelength, the dipoles' diameter is $d = 1$ mm, $L = 3$ mm, and $R = 750$ mm.

The following section deals with numerical validations.

IV. NUMERICAL VALIDATIONS

Let us now consider a set of dipoles having an identical length of $L = 3$ mm and a diameter of $d = 1$ mm. The dipoles are located over a source radius of $R = 750$ mm.

The scheme of Fig. 4 is followed to compute the two wavefield sets based on (11a) – (11b). Computation includes the following array sizes $N = 3, 5$, and 7 for a test zone size of $r = 0.1R$. The theoretical results are compared with simulations obtained from both CST using the Finite Integration Technique (FIT) [8] and HFSS using the Finite Element Method (FEM) [9]. Comparisons include various frequencies, typically 0.4 GHz, 0.8 GHz, and 1.2 GHz. Table 3 summarizes the corresponding electrical sizes of the source (array) and test zone radii.

The dipoles are physically designed and simulated in phase with equal amplitude according to Fig. 5a–5b. The E- and H-field components are recorded over the test zone without far-field approximation as near-fields.

Figs. 6 and 7 depict the results of the E- and H-field components for the case of $N = 3$ for θ - and ϕ -polarizations, respectively. The cases of $N = 5$ and 7 are shown in Figs. 8 and 9, and Figs. 10 and 11, respectively.

Figs. 6–11 shows that the theoretical results positively correlate with FIT and FEM for the two wavefield polarization sets for all N and frequency values. However, it is seen, for the θ -polarized wavefields, that the E-field theoretical results get more accurate as frequency increases, but the H-field results remain conveniently accurate regardless of frequency.

Indeed, on the one hand, the θ -polarized E-field is fairly accurate for $R < 3\lambda$ because each dipole does not rigorously radiate exclusive spherical waves in this range. This is explained by the non-negligible radial E-field component ($E_{rn} \neq 0$) that carries evanescent waves. However, spherical waves establish almost exclusively for $R \geq 3\lambda$ as E_{rn} gets negligible, which fits the approach's assumption. Furthermore, on the other hand, the theoretical H-field results remain conveniently accurate for the entire range of $R \geq \lambda$ as H_{rn} vanishes (exclusive spherical waves). A similar analysis can be made for the ϕ -polarized wavefield components by interchanging E with H. Finally, it is worth mentioning that

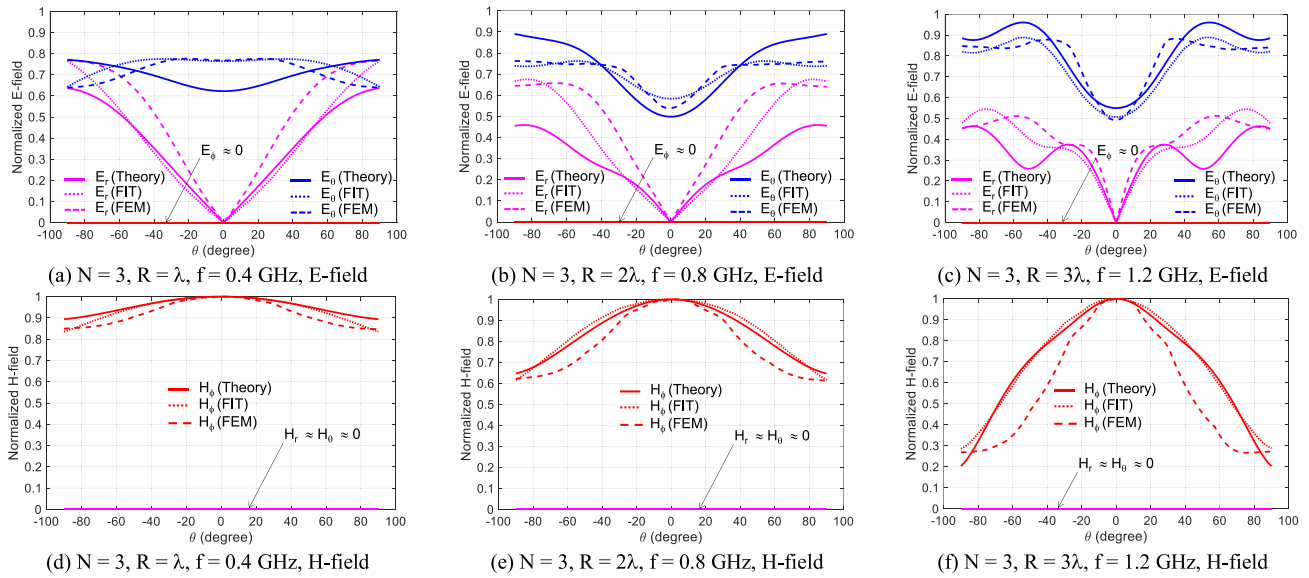


FIGURE 6. Theoretical and simulated electric and magnetic field components of the θ -polarized wavefield for $N = 3$ and $r = 0.1R$.

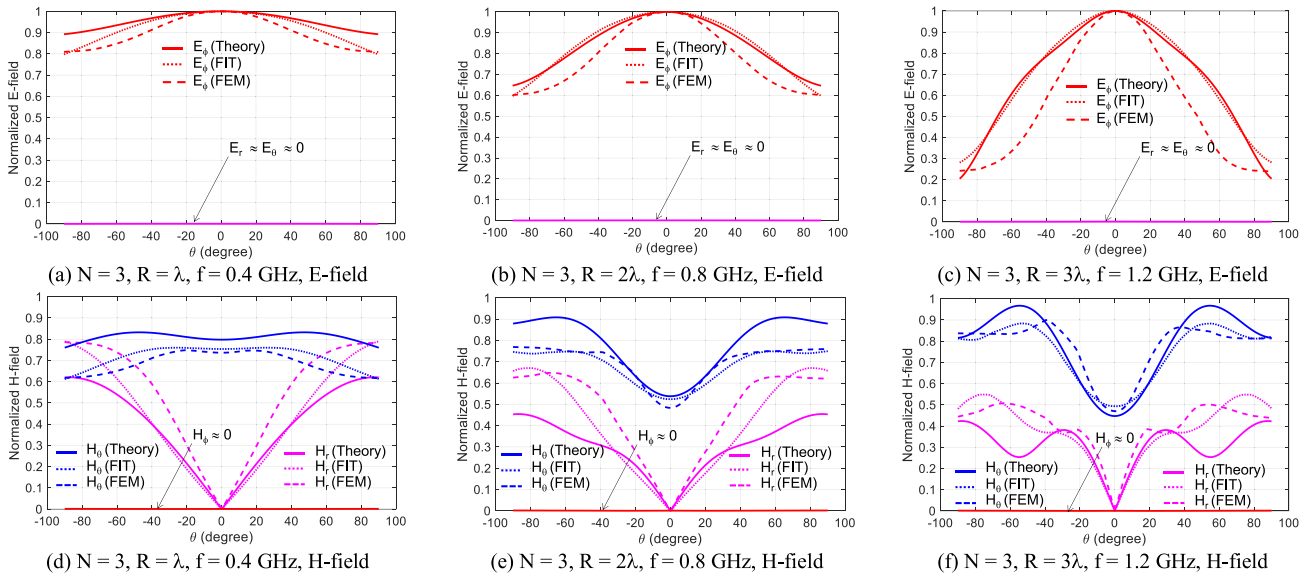


FIGURE 7. Theoretical and simulated electric and magnetic field components of the ϕ -polarized wavefield for $N = 3$ and $r = 0.1R$.

further simulations show that the dipoles' physical diameter does not affect the results, considering thin and moderately thick dipoles (typically, $L/d \geq 3$).

Overall, the differences between the theoretical results and simulations remain acceptable and comparable to those noticed between the two full-wave results themselves.

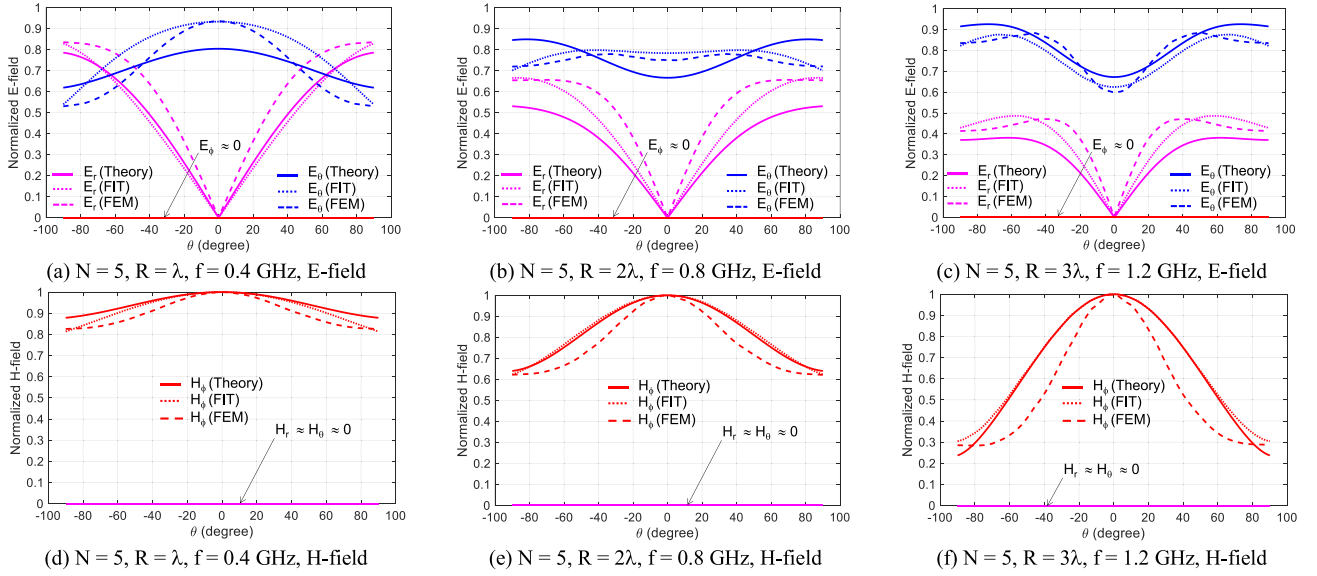
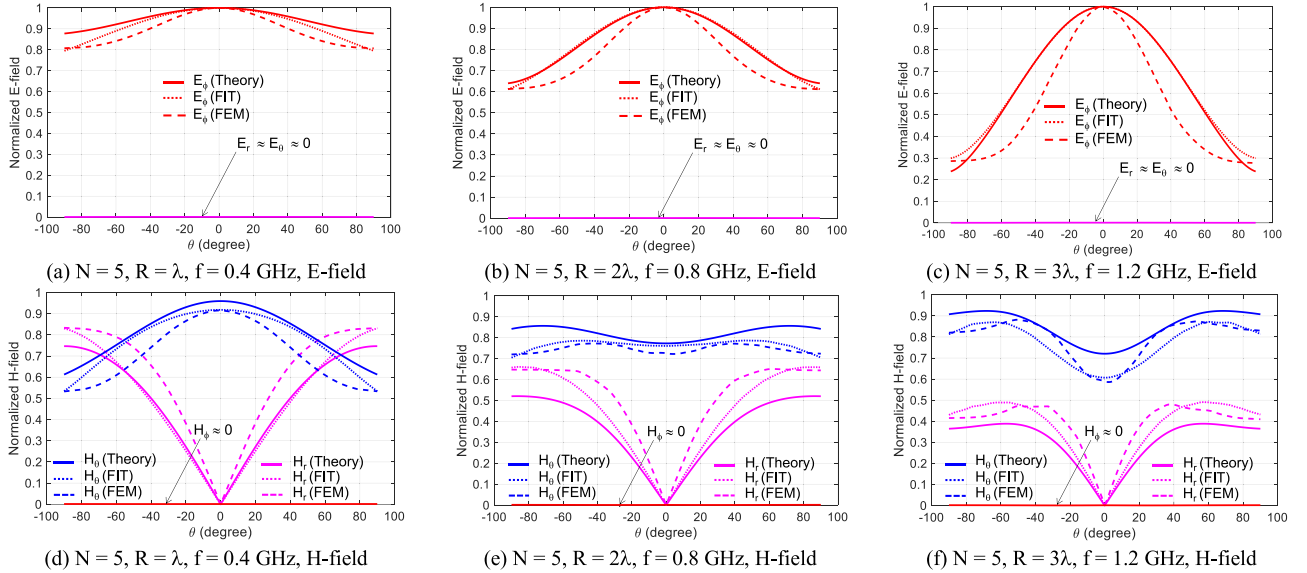
Beyond, one can notice that the θ -polarized wavefield set effectively shows no electric field component in the azimuthal plane ($E_\phi = 0$), while both radial (E_r) and vertical (E_θ) electric components are present. Thus, E_r exists in the receiving coordinate system, even though it may not exist locally in each dipole's coordinate system. The magnetic field component H_ϕ exists, while $H_r \approx H_\theta \approx 0$. In sum, the dipoles tend to radiate plane waves individually in

the far-zone (TEM mode). Still, their spatial orientations turn this propagation mode into a transverse electric mode (TE^ϕ mode) in the receiving system.

The ϕ -polarized wavefield set shows $E_r \approx E_\theta \approx 0$, while $E_\phi \neq 0$ as expected. The magnetic field shows $(H_r, H_\theta) \neq 0$ and $H_\phi \approx 0$, which complies with a transverse magnetic mode (TM^ϕ mode).

The ϕ -polarized electric wavefield becomes more directive as frequency increases, explained by a general antenna's directivity increase with frequency. However, a wavier behavior with frequency is seen for the θ -polarized electric wavefield.

The array factor effect is not sensitively visible on the ϕ -polarized electric wavefield, showing an almost steady


 FIGURE 8. Theoretical and simulated electric and magnetic field components of the θ -polarized wavefield for $N = 5$ and $r = 0.1R$.

 FIGURE 9. Theoretical and simulated electric and magnetic field components of the ϕ -polarized wavefield for $N = 5$ and $r = 0.1R$.

behavior with N . In contrast, the θ -polarized electric wavefield is more directive with N .

The two wavefield sets have interchanged field components. Indeed, the E-field components of the θ -polarized wavefield behave almost the same as the H-field components of the ϕ -polarized wavefield, and vice versa. Hence, it is obvious to extend the E-field analysis above to the corresponding H-fields.

Fig. 12 shows the coupling between the adjacent dipoles for the array case of seven dipoles for the θ -polarized wavefield.

As seen in Fig. 12, the coupling between the dipoles is below -130 dB up to 2 GHz. This negligible coupling level for the θ -polarized wavefield set also stands for the ϕ -polarized wavefield, confirming the use of (11a) – (11b)

as the “correct” radiation characteristics of each dipole taken in the lattice.

The following section discusses the question of synthesizing isotropic wavefields in θ - and ϕ -polarizations.

V. SYNTHESIS OF ISOTROPIC WAVEFIELDS

This section investigates the question of creating an isotropic wavefield in both θ - and ϕ -polarizations, typically verifying the criterion of an error vector magnitude (EVM) equal to or smaller than -30 dB as considered in [6]. Since the propagation modes of the θ - and ϕ -polarized wavefields are not transverse electromagnetic (TEM), but TE^ϕ and TM^ϕ , respectively, this criterion is applied to the power density rather than the electric field solely.

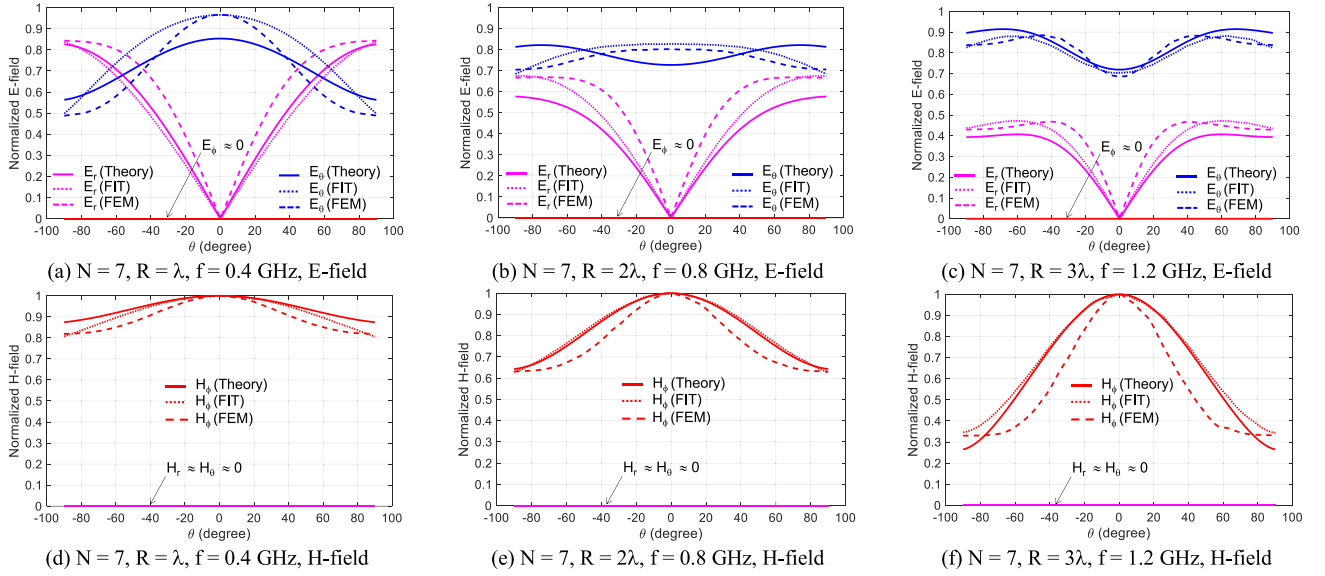


FIGURE 10. Theoretical and simulated electric and magnetic field components of the θ -polarized wavefield for $N = 7$ and $r = 0.1R$.

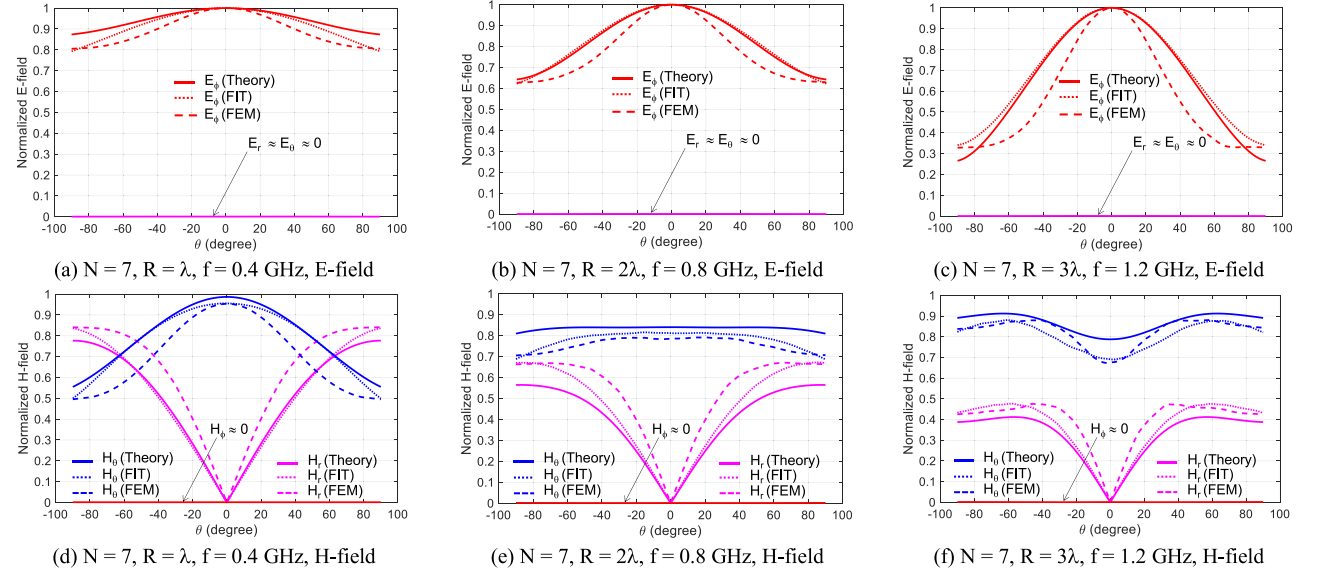


FIGURE 11. Theoretical and simulated electric and magnetic field components of the ϕ -polarized wavefield for $N = 7$ and $r = 0.1R$.

The power density function (PDF) is expressed with the Poynting vector (S) as follows:

$$PD = \Re(S) = \frac{1}{2} \Re(\mathbf{E} \times \mathbf{H}^*) \quad (13a)$$

$$PDF = \frac{|PD|}{\max(|PD|)} \quad (13b)$$

where \Re means taking the real part, symbol $*$ denotes the complex conjugate.

The averaged EVM applies to PDF as follows:

$$EVM_{pdfavg}(dB) = 10 \log \left(\frac{\int_{\Omega} |PDF(\Omega) - PDF_{ref}(\Omega)|^2 d\Omega}{\int_{\Omega} |PDF_{ref}(\Omega)|^2 d\Omega} \right). \quad (14)$$

In (14), PDF_{ref} denotes the reference or targeted power density function. For an isotropic wavefield, which is targeted in this section, $PDF_{ref} = 1$.

A. POWER DENSITY AMPLITUDE

First, let us analyze the power density peak amplitude computed from (13a) as a function of N for several R values, considering a test zone of $r = 0.1R$ as depicted in Fig. 13 for the θ -polarized wavefield. The case of $N = 1$ normalizes the y-axis values in Fig. 13.

Fig. 13 shows an increase of the power density peak amplitude with N , as expected. However, the case of $N = 2$ produces a deep, explained by a mutual pattern compensation (destructive interference) for the two dipoles located

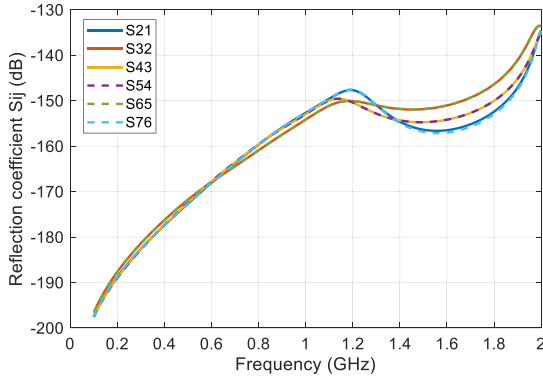


FIGURE 12. Simulated reflection coefficient (mutual coupling) of the 7-dipole array synthesizing the θ -polarized wavefield. The dipoles are labeled #1 up to #7 from the left- to the right-hand sides in Fig. 5a–5b.

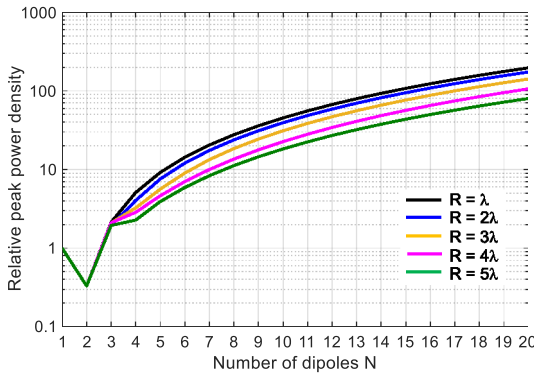


FIGURE 13. Power density peak amplitude computed from (12a) as a function of N for several values of R with $r = 0.1R$. The case of $N = 1$ normalizes the y-axis values.

symmetrically in opposite positions ($\theta_{cn} = \pm 90^\circ$). The ϕ -polarized wavefield shows a similar result. For this reason, the following analysis excludes the case of $N = 2$.

B. ACCURACY AND SIZE OF THE TEST ZONE

Let us compute the average error vector magnitude on the power density function (14), denoted EVM_{pdfavg} , as a function of the ratio r/R for several values of R with $r = 0.1R$ and $N = 3$. Figs. 14a and 14b show the results for the θ - and ϕ -polarized wavefields, respectively, where the $EVM_{pdfavg} = -30$ dB criterion is the targeted accuracy.

Figs. 14a and 14b show a monotonically increasing error with ratio r/R , meaning that the wavefields remain isotropic, even improve as r/R decreases. This behavior is quite interesting, indicating the existence of a maximum test zone size under which the test zone remains isotropic, typically a half-disk with a maximum radius of r_{max} . Under $EVM_{pdfavg} \leq -30$ dB, $r_{max} \approx 0.086R$, $0.053R$ and $0.038R$ for $R = \lambda$, 2λ , and 3λ , respectively, for the θ -polarized wavefield. Similarly, the ϕ -polarized wavefield provides $r_{max} \approx 0.022R$ for R ranges between λ and 5λ .

Following Fig. 14a–14b calculations under $EVM_{pdfavg} \leq -30$ dB, one can compute the upper bound of the test zone (r_{max}/λ) as a function of the source radius (R/λ). Figs. 15a

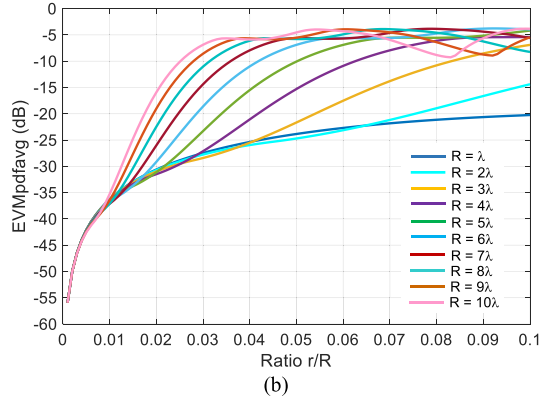
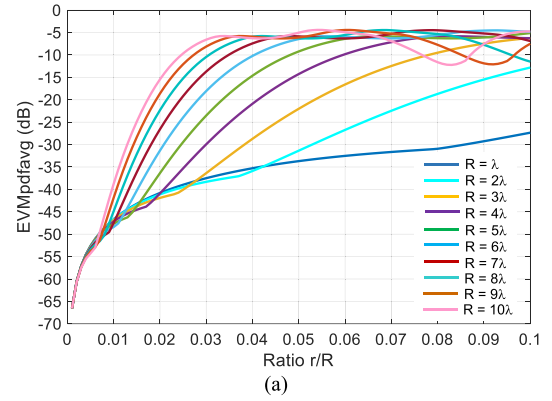


FIGURE 14. Average error vector magnitude for the power density function EVM_{pdfavg} as a function of the ratio r/R for several values of R with $r = 0.1R$ and $N = 3$, (a) θ -polarized wavefield, (b) ϕ -polarized wavefield.

and 15b show these results for the θ - and ϕ -polarized wavefields, respectively, for several N values.

Figs. 15a and 15b show that the case of $N = 3$ provides the largest test zone for both polarizations with r_{max} ranges between 0.07λ and 0.13λ for $R \geq 3\lambda$. Simulations confirm this result and set r_{max} between 0.08λ and 0.13λ for $N = 3$.

Thus, in practice, one should consider the case of three dipoles located at $\theta_{cn} = \{-90^\circ, 0, +90^\circ\}$, and set the source radius as $R \geq 5\lambda$ to get the most extensive isotropic test area with $r \leq r_{max} \approx 0.1\lambda$. This area is suitable for a general antenna, a single or an array, with a size of $D \leq \lambda/5$, where D is the diameter of the antenna's smallest virtual sphere. This area size is not essentially limiting for antenna testing as most antennas are half- or quarter-wavelength. A slight size reduction (folding, substrate permittivity or permeability, etc.) may help fit this size constraint for a single antenna case. However, antenna arrays may require a significant size reduction or investigating larger test zones using other transmitting antenna types, even with arbitrary feeding.

The following section uses the synthesized isotropic wavefields to predict the performance of a test antenna.

VI. APPLICATION: PERFORMANCE OF A FOLDED DIPOLE

This section intends to apply the synthesized isotropic wavefields to a test antenna directly inside the antenna simulator. The objective is to predict the antenna's

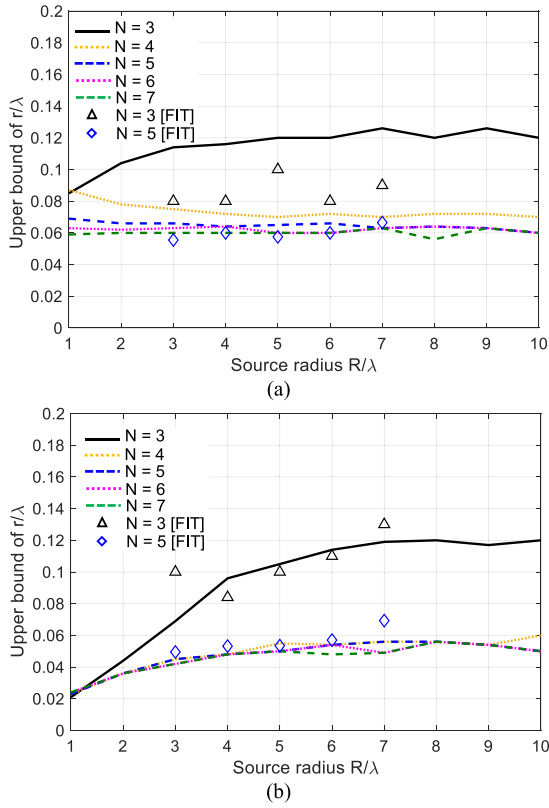


FIGURE 15. Upper bound of the test zone (r_{\max}/λ) as a function of the source radius electrical size (R/λ) for several values of N , (a) θ -polarized wavefield, (b) ϕ -polarized wavefield.

performance within a complex propagation medium supporting non-line-of-sight (NLOS) propagations and multiple incidences [10]–[13]. These kinds of propagation media include mobile communications over which ambient RF energy harvesting has attracted much attention. Predicting, for instance, the power that would receive an antenna operating in this context is of particular interest. Thus, the focus will be on the ambient RF energy harvesting application, even though predicting the received power finds interest in many other applications.

According to several studies [14]–[15], most of the available ambient RF power densities come from GSM downlink bands, providing an average power density ranging between 1 and 40 nW/cm². Thus, the question is: how much can receive an antenna operating in this medium? For ambient energy harvesting options, anticipating this question is essential for designing an efficient *rectenna* system (antenna + rectifier + power management circuit). The first advantage is knowing the power at the antenna's terminals and comparing it with the rectifier's sensitivity, which helps choose the appropriate diode or predict signals detection. The second advantage is anticipating the output DC (direct current) power based on the rectifier's conversion efficiency. Then, comparing this DC power with the cold start power of the power management circuit can predict the system's operation. Finally, all these predictions will be possible during the design stage with a standard antenna simulator.

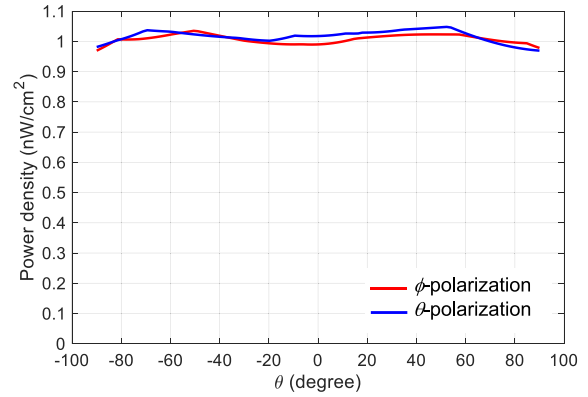


FIGURE 16. Power densities of the 2-D isotropic wavefields synthesized inside the antenna simulator (CST) considering $N = 3$, $R = 5\lambda$, and $r_{\max} \approx 0.1\lambda$. The dipoles are fed in phase with equal amplitude.

A. 2-D ISOTROPIC WAVEFIELD SYNTHESIS INSIDE THE ANTENNA SIMULATOR

The time average behavior of GSM downlink propagation signals is often Gaussian or isotropic in both indoor and outdoor environments [12], [15]. Since a Gaussian wavefield is simplistic to synthesize, feasible with a single directive antenna, the focus will be on isotropic.

Let us assume a random propagation medium (*Rayleigh-type*) with a time-averaged power density of $PD_{\text{avg}} = 1 \text{ nW/cm}^2$ in both polarizations for all directions. Then, according to Section V, the optimum dipole array that can synthesize the corresponding wavefields with the largest isotropic test zone is the case of $N = 3$ with $R \geq 5\lambda$ and $r \leq r_{\max} \approx 0.1\lambda$.

Let us implement these optimum wavefield sets inside the antenna simulator. Two simulations are needed to set the power density of the wavefield to the targeted value (PD_{avg}) in each polarization. The dipoles' current amplitudes are set to unity in the first simulation to get the initial value of the power density (PD_0). In the second simulation, the dipoles' current amplitudes are adjusted to $\sqrt{(PD_{\text{avg}}/PD_0)}$. Fig. 16 shows the calibrated wavefields in CST.

Fig. 16 shows a steady power density regardless of the incidence angle θ with a value around 1 nW/cm² for each synthesized wavefield as expected. The cross-polarization ratio (XPR) is close to unity regardless of θ , $XPR \approx 1$. One may set another value for XPR following the previous calibration process with a different target value for PD_{avg} for both polarizations.

B. CASE OF 2-D ISOTROPIC WAVEFIELDS

Let us consider a folded dipole as the antenna under test (AUT), operating at 2 GHz. The folded dipole is printed on a 0.635mm-thick Rogers RT6006 substrate with a permittivity of $\epsilon_r = 6.45$ and a loss tangent of $\tan\delta = 0.0027$, specified at 10 GHz. Fig. 17 shows the antenna's schematic view and simulated reflection coefficient (S_{11}), while Table 4 summarizes its dimensions and performances obtained in the transmitting mode.

The synthesized wavefields of Fig. 16 individually illuminate the folded dipole loaded by a 50 Ω -load. Rotating

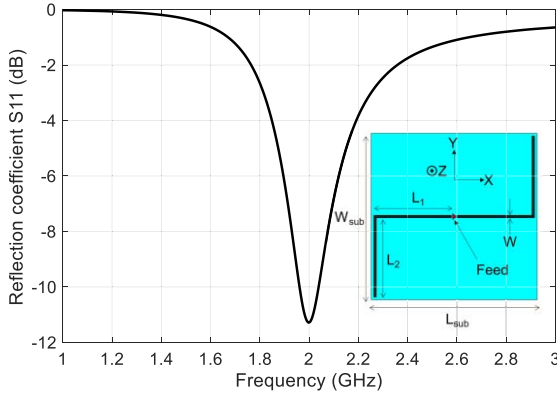


FIGURE 17. Simulated reflection coefficient (S_{11}) of the folded dipole.

TABLE 4. Dimensions and performances of the folded dipole at 2 GHz.

Characteristics	Values
Dimensions (mm)	$L_1 = 14.25$ $L_2 = 15$ $W = 0.5$ $L_{sub} = W_{sub} = 31.5$
Peak directivity (dBi)	1.88
Peak realized gain (dBi)	1.5
Efficiencies	Radiation : 99%, Total : 92%

Performance data are obtained with CST in the transmitting mode.

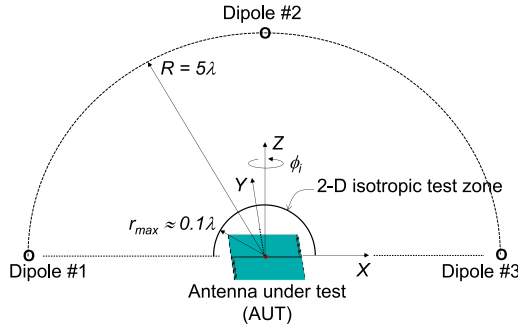


FIGURE 18. Schematic view of the folded dipole (AUT) under illumination by the synthesized 2-D isotropic wavefield inside the antenna simulator (CST), considering $N = 3$, $R = 5\lambda$ and $r_{max} \approx 0.1\lambda$.

either the wavefields or the folded dipole over a 180° -range around the z -axis will create a 3-D isotropic test zone sequentially (Fig. 18). Let us rotate the wavefields by angle ϕ_i varying every $\Delta\phi_i = 10^\circ$, for instance. Fig. 19 depicts the received power as a function of angle ϕ_i for both polarizations.

It is seen that the folded dipole captures both polarization powers differently and shows two deeps at $\phi_i = 20^\circ$ and 120° for the ϕ - and θ -polarizations, respectively. For $0 \leq \phi_i < 10^\circ$ and $40^\circ < \phi_i \leq 180^\circ$, the folded dipole captures more power in ϕ -polarization than in θ -polarization. The profiles of the received powers in Fig. 19 perfectly match with the antenna peak realized gains in both polarizations with the azimuth angle ϕ , as seen in Fig. 20.

C. CASE OF 3-D ISOTROPIC WAVEFIELDS

Since the 3-D isotropic wavefield may be obtained through 180° -range sequential rotations of the 2-D isotropic wavefield, one can integrate (12a) over the upper hemisphere

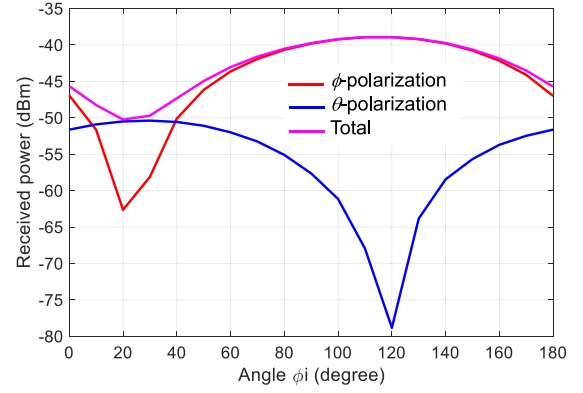


FIGURE 19. Received powers of the folded dipole at 2 GHz as a function of angle ϕ_i . The antenna is sequentially illuminated by two 2-D isotropic wavefields of 1 nW/cm^2 power density.

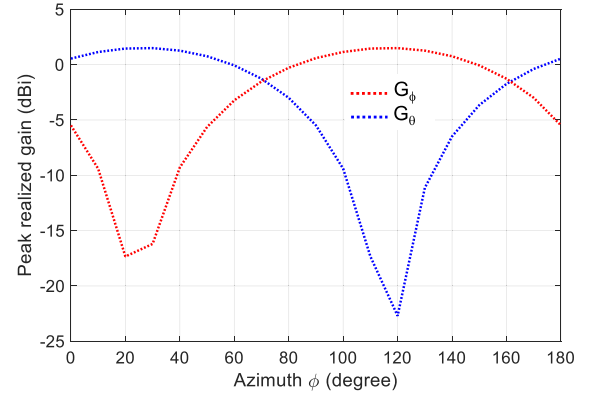


FIGURE 20. Peak realized gain of the folded dipole at 2 GHz as a function of the azimuth angle ϕ . The results are obtained in the transmitting mode.

surface (Σ_{top}) of radius $r_{max} \approx 0.1\lambda$ to get the 3-D available powers in both polarizations, typically $P_{0\theta}$ and $P_{0\phi}$. Similarly, one can integrate the received powers in both polarizations as a function of angle ϕ_i to get the 3-D received powers, typically $P_{rec\theta}$ and $P_{rec\phi}$.

From these computations that are straightforward to implement inside most antenna simulators, one can derive the total received power (P_{rec}) and the mean effective gain (MEG) as follows:

$$P_{rec} = P_{rec\theta} + P_{rec\phi} \quad (15a)$$

$$MEG = \frac{P_{rec}}{P_0} = \frac{P_{rec\theta} + P_{rec\phi}}{P_{0\theta} + P_{0\phi}} \quad (15b)$$

where

$$P_{recp} = \int_0^\pi P_{recp}(\phi_i) d\phi_i \quad (16a)$$

$$P_{0p} = \int_{\Sigma_{top}} \underbrace{|\mathbf{PD}|}_{p\text{-polarized wavefield}} d\Sigma$$

$$= 2\pi r_{max}^2 \int_{-\pi/2}^{\pi/2} |\mathbf{PD}_p(\theta)| d\theta \quad (16b)$$

In (16a) – (16b), subscript p denotes the θ - and ϕ -polarized wavefields. In the right-hand side of (16b), factor “2” is added to compensate for “1/2” in (13a).

TABLE 5. Predicted performances of the folded dipole at 2 GHz under 3-d isotropic wavefields in both θ - and ϕ -polarizations.

	θ -polarization	ϕ -polarization	Total
Received power (dBm)	-48.14	-36.91	-36.60
Available power (dBm)	-38.76	-38.80	-35.77
MEG (dBi)	Basic calculation [18]		-0.24
	Proposed		-0.83

The basic MEG calculation is obtained by post-processing using the far-field pattern of the antenna in transmitting mode for a cross-polarization ratio of $XPR = 1$. In the proposed analysis, the antenna is in receiving mode, illuminated in both polarizations by isotropic wavefields of 1 nW/cm^2 power density. Integrations are performed over the upper hemisphere surface (Σ_{top}) of radius $r_{max} \approx 0.1\lambda$.

Computation of (15a) – (15b) based on (16a) – (16b) and Figs. 16 and 19 provide the results in Table 5. The “basic” MEG result is obtained by post-processing [12]–[13] using the far-field pattern of the antenna in transmitting mode with $XPR = 1$.

According to Table 5, the folded dipole receives -36.6 dBm from the available power of -35.77 dBm illuminating it with isotropic wavefields in both polarizations under a power density of 1 nW/cm^2 . This provides a MEG of -0.83 dBi , close to -0.24 dBi obtained through far-field post-processing. The difference is due to a slight under-estimation of P_{rec} (16a) due to the step angle $\Delta\phi_i = 10^\circ$; Lowering $\Delta\phi_i$ could improve the results at the cost of higher simulation time.

In the ambient RF energy harvesting context, the received power level indicates that the folded dipole can harvest enough power within an averaged time to switch on the rectifier as long as its build-in Schottky diode’s sensitivity is smaller than -36.6 dBm . For instance, the HSMS2860 diode with a sensitivity around -55 dBm up to 5.8 GHz may be used. Furthermore, the designer can anticipate the output DC power level based on the conversion efficiency. Beyond that, the entire rectenna (antenna + rectifier) may be optimized directly inside the full-wave simulator under the wavefield illumination to anticipate the performance data more accurately. In addition, array theory approaches may be associated with this design methodology to deal with larger antennas as arrays of harvesters.

VII. CONCLUSION

This paper has dealt with a 2-D wavefield synthesis approach directly implementable in standard antenna simulation tools. The approach, implemented with thin electric dipoles for their simple geometry, used a field transformation matrix and two array sets to synthesize vertically and horizontally polarized wavefields. The synthesized wavefields are validated numerically with full-wave simulations (FIT, FEM) over various array sets (size, number, polarization, frequency).

Further analysis demonstrated the synthesis of 2-D isotropic wavefields in both polarizations over the largest test zone radius of $r_{max} \approx \lambda/10$ using three dipoles located

at $R \geq 5\lambda$ far from the phase center. Application to a test antenna (folded dipole) anticipated the received power and MEG directly inside the antenna simulator.

REFERENCES

- [1] C. A. Balanis, *Antenna Theory Analysis and Design*, 3rd ed. Hoboken, NJ, USA: Wiley, 2005.
- [2] X. Chen, “Throughput modeling and measurement in an isotropic-scattering reverberation chamber,” *IEEE Trans. Antennas Propag.*, vol. 62, no. 4, pp. 2130–2139, Apr. 2014.
- [3] W. Fan *et al.*, “A step toward 5G in 2020: Low-cost OTA performance evaluation of massive MIMO base stations,” *IEEE Antennas Propag. Mag.*, vol. 59, no. 1, pp. 38–47, Feb. 2017.
- [4] W. Yu, Y. Qi, K. Liu, Y. Xu, and J. Fan, “Radiated two-stage method for LTE MIMO user equipment performance evaluation,” *IEEE Trans. Electromagn. Compat.*, vol. 56, no. 6, pp. 1691–1696, Dec. 2014.
- [5] P. Kyösti, W. Fan, G. F. Pedersen, and M. Latva-Aho, “On dimensions of OTA setups for massive MIMO base stations radiated testing,” *IEEE Access*, vol. 1, pp. 335–349, 2016.
- [6] C. Schirmer *et al.*, “3D wave-field synthesis for testing of radio devices,” in *Proc. EuCAP*, 2014, pp. 3394–3398.
- [7] P. Kyösti, T. Jämsä, and J.-P. Nuutinen, “Channel modelling for multi-probe over-the-air MIMO testing,” *Int. J. Antennas Propag.*, vol. 2012, May 2012, Art. no. 615954.
- [8] “CST Computer Simulation Technology.” [Online]. Available: www.cst.com (Accessed: Jul. 2021).
- [9] “High-Frequency Structure Simulator.” [Online]. Available: <http://www.ansys.com/> (Accessed: Jul. 2021).
- [10] T. S. Rappaport, *Wireless Communications: Principles and Practice*. London, U.K.: Pearson, 2002.
- [11] W. C. Jakes, *Microwave Mobile Communications*. New York, NY, USA: Wiley, 1974.
- [12] T. Taga, “Analysis for mean effective gain of mobile antennas in land mobile radio environments,” *IEEE Trans. Veh. Technol.*, vol. 39, no. 2, pp. 117–131, May 1990.
- [13] A. A. Glazunov, A. F. Molisch, and F. Tufvesson, “Mean effective gain of antennas in a wireless channel,” *IET Microw. Antennas Propag.*, vol. 3, no. 2, pp. 214–227, Mar. 2009.
- [14] M. Piñuela, P. D. Mitcheson, and S. Lucyszyn, “Ambient RF energy harvesting in urban and semi-urban environments,” *IEEE Trans. Microw. Theory Techn.*, vol. 61, no. 7, pp. 2715–2726, Jul. 2013.
- [15] S. Aghabeiki, “Récupération de l’énergie électromagnétique ambiante pour l’amélioration de l’autonomie des objets communicants,” Ph.D. dissertation, ESIGELEC IRSEEM, Université Rouen Normandie, Rouen, France, Dec. 2020.

CONSTANT M. A. NIAMIEN (Member, IEEE) received the M.Sc. and Ph.D. degrees in electrical engineering from the University of Rennes1, Rennes, France, in 2007 and 2010, respectively, and the “Habilitation à Diriger la Recherche” degree from the University of Rouen, France, in 2020.

He was with the Department of Antennas and Propagation, Centre of Nuclear Energy, Grenoble, France, as a Research Engineer in 2011. He was with the LEMA, EPFL, Switzerland, in 2010 as an Invited Researcher. In 2012, he joined EMITECH Group, Montigny-le-Bretonneux, France, as an Engineer. He joined ESIGELEC, IRSEEM, Normandie University, UNIROUEN, Rouen, France, as an Associate Professor in 2012. He has been a Full Professor with ESIGELEC since December 2020. He has coauthored of a French patent and published more than 50 journal and conference papers edited by IEEE and IET societies. His research fields include multiband and broadband antennas, antenna theory, electromagnetic modeling for antenna applications, receiving antennas, metasurfaces, and rectennas for wireless and ambient energy harvesting applications.

Prof. Niamien has been the project coordinator of three research projects (European, Regional) for an overall budget of more than 3.5 M€ and a scientific contributor of two research projects. He has Co-Chaired two IEEE Conference (APS, APMC) sessions. He has been a member of the European Association on Antennas and Propagation since 2015 and a TPC Member of the *Journées Nationales Microondes* (JNM19) Caen, France.